Material Effects on Electron-Capture Decay in Cryogenic Sensors

Amit Samanta,[1] Stephan Friedrich,[1] Kyle G. Leach,[2] and Vincenzo Lordi[1,*]

[1] *Lawrence Livermore National Laboratory, 7000 East Avenue, Livermore, California 94550, USA*

[2] *Colorado School of Mines, 1500 Illinois Street, Golden, Colorado 80401, USA*

(Received 5 June 2022; accepted 14 November 2022; published 10 January 2023)

Several current searches for physics beyond the standard model are based on measuring the electron-capture (EC) decay of radionuclides implanted into cryogenic high-resolution sensors. The sensitivity of these experiments has already reached the level where systematic effects related to atomic state energy changes from the host material are a limiting factor. One example is a neutrino mass study based on the nuclear EC decay of ^{7}Be to ^{7}Li inside cryogenic Ta-based sensors. To understand the material effects at the required level, we use density-functional theory to model the electronic structure of lithium atoms in different atomic environments of the polycrystalline Ta absorber film. The calculations reveal that the Li 1*s* binding energies can vary by more than 2 eV due to insertion at different lattice sites, at grain boundaries, in disordered Ta, and in the vicinity of various impurities. However, the total range of Li 1*s* shifts does not exceed 4 eV, even for extreme amorphous disorder. Furthermore, when investigating the effects on the Li 2*s* levels, we find broadening of more than 5 eV due to hybridization with the Ta band structure. Material effects are shown to contribute significantly to peak broadening in Ta-based sensors that are used to search for physics beyond the standard model in the EC decay of ^{7}Be, but they do not explain the full extent of observed broadening. Understanding these in-medium effects will be required for current- and future-generation experiments that observe low-energy radiation from the EC decay of implanted isotopes to evaluate potential limitations on the measurement sensitivity.

DOI: 10.1103/PhysRevApplied.19.014032

I. INTRODUCTION

Some of the most accurate measurements of nuclear decays can be made by embedding radionuclides of interest in cryogenic high-resolution radiation sensors. These state-of-the-art detection methods are capable of electronvolt-scale resolution and allow the total energy of nuclear decay, including daughter recoil and atomic de-excitations, to be measured with great precision. This approach is used to great effect in the current generation of searches for physics beyond the standard model (BSM) in the neutrino sector [1–3]. In these experiments, ultrahigh-sensitivity measurements of the low-energy nuclear-decay products are performed to reconstruct the missing momenta that would result from heavy-neutrino mass states.

Three experiments of this type are currently active that use the nuclear electron-capture (EC) decay of ^{163}Ho or ^{7}Be radioisotopes embedded in either magnetic microcalorimeters [1], transition-edge sensors [2], or superconducting tunnel junctions (STJs) [3]. The high energy resolution of these cryogenic detectors provides the required sensitivity in the search for BSM physics. This feature also makes these experiments sensitive to the chemical shifts due to interactions between the radioisotope's atomic shell and the matrix material into which it is embedded. Effects of this nature are so small that they have traditionally been neglected in decay experiments due to the large difference in energy scales for nuclear processes and chemical shifts. Here, we show that this is no longer possible for experiments sensitive to energies and masses on the eV scale or below, where these effects become significant—specifically, in the case of ^{7}Be decay in Ta-based STJ detectors.

The Beryllium-7 Electron capture in Superconducting Tunnel junctions (BeEST) experiment is a search for BSM physics in the neutrino sector using ^{7}Be implanted into Ta-based STJs [3,4]. When ^{7}Be decays by EC to ^{7}Li and an electron neutrino inside of the thin-film STJ, the neutrino escapes, and the kinetic energy of the recoiling ^{7}Li daughter atom can be measured with high precision. The core hole produced by the capture of the bound electron relaxes on the timescale of a few femtoseconds [5], i.e., significantly faster than the about 1-μs rise time of the STJ sensor signal, so that the core-hole energy is simply added to the ^{7}Li recoil signal. The resulting low-energy decay spectrum, therefore, consists of four peaks due to EC from the ^{7}Be 1*s* shell (*K* capture) or the ^{7}Be 2*s* shell

*lordi2@llnl.gov

(L capture) into the ground state or the first excited state of ^{7}Li (Fig. 1). Any admixture of a heavy-BSM-neutrino mass state, or, in fact, any new massive particle that couples to the decay, would reduce the recoil energy and add a shifted ^{7}Li spectrum at lower energies as a signature.

The absorber films in the STJ sensors of the BeEST experiment consist of polycrystalline Ta in the body-centered cubic (bcc) phase deposited by sputtering [4]. Radioactive ^{7}Be nuclei (half-life ~ 53 days) are produced via the isotope-separation-online (ISOL) technique [6] and implanted at an energy of 24 keV through a Si collimator to an average depth of about 55 nm [3,4]. The ISOL production process also introduces a stable ^{7}Li contaminant into the beam with roughly 50 times higher intensity than that of ^{7}Be, which is simultaneously implanted into Ta with the same depth profile.

Matrix-dependent effects are suggested by the observation that the EC decay peaks in the recoil spectrum are broadened well beyond the intrinsic energy resolution of the STJ (Fig. 1, black) [4]. The K-shell capture peak at 107 eV has a width of 6.7 eV full-width at half-maximum (FWHM), and the L-shell capture peak at 57 eV is even broader, with a width of 8.2 eV FWHM. In contrast, the pulsed-laser calibration spectrum (Fig. 1, gray), which consists of a comb of peaks due to an integer number of absorbed laser photons, shows the expected detector resolution of about 2 eV FWHM in the same energy range. Both spectra are taken with the same STJ sensor at the same time under identical conditions, with the calibration recorded in coincidence with the laser trigger and the EC spectrum in anticoincidence. This broadening of the EC spectrum beyond the calibration signal is critically significant for the BeEST experiment, because it affects the measurable spectral shifts and thus currently limits the sensitivity in the search for neutrinos with masses below 100 keV/c^2, where their relevance as dark-matter candidates is highest [7].

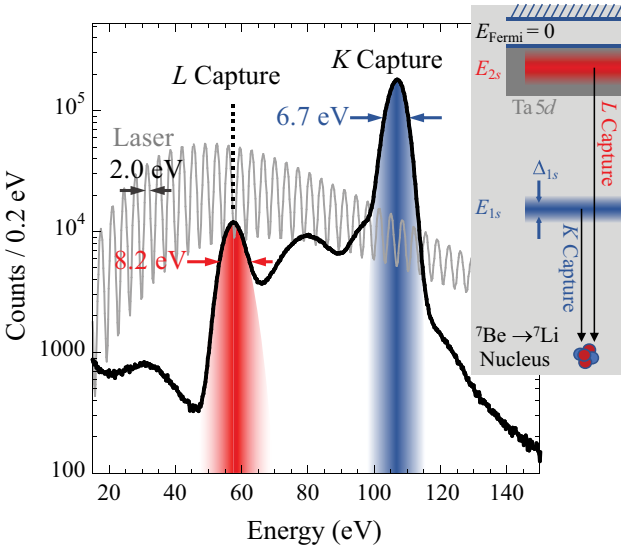

FIG. 1. EC spectrum of ^{7}Be implanted into Ta-based STJ detectors [3]. Energies from relaxation of the 1s (blue) or 2s (red) core hole add to the ^{7}Li recoil energy. Inset illustrates how variations of Δ_{1s} and Δ_{2s} in the ^{7}Li 1s and 2s binding energies can broaden the EC peaks beyond the resolution of the laser calibration spectrum (gray).

Although the source of the full broadening effect is unknown, it could be caused by variations of the core-hole energies that are added to the recoil (Fig. 1, inset). This is the subject of this work. Generally, for atoms embedded in a material, the core-hole energies can change due to structural differences of the local sites in the host matrix, hybridization of defect states with the orbitals of the matrix materials, or impurities that affect the local crystal field. A systematic analysis of the relative contributions from these three effects is needed to understand the sources of peak broadening and to improve the design of the detectors and the experiment. For a direct comparison with recent observations [3,4], the first system we choose to study is that of ^{7}Be EC decay in tantalum.

This paper examines the range of ^{7}Li 1s and 2s binding energies at different sites in a polycrystalline Ta matrix. Since these effects cannot easily be disentangled experimentally, we use density-functional theory (DFT) calculations to estimate their relative contributions to the observed peak broadening. The implantation process is very dynamic and can impart nonequilibrium atomic configurations into the sample. For the current generation of devices, no annealing is used to attempt to heal the lattice after implantation. Here, we consider a variety of plausible atomic environments to explore the range of their effects on capture peak broadening. We focus on ^{7}Li because relaxation of the core hole occurs after the EC decay of ^{7}Be to ^{7}Li. In Sec. III A, the Li 1s binding energies at substitutional and interstitial sites of the bcc Ta lattice are calculated as reference cases for K capture. Section III B then estimates the influence of structural disorder at grain boundaries and locally amorphous sites on the Li 1s energies, and Sec. III C extends the simulations to impurities that are commonly found in sputtered Ta films. Section III D discusses the influence of these effects on the Li 2s levels involved in L-capture events. Finally, we summarize the consequences of the results for high-accuracy BSM physics experiments based on the electron-capture decay of ^{7}Be to ^{7}Li in superconducting sensors and how this work indicates that such effects must be evaluated for experiments of this type.

II. COMPUTATIONAL DETAILS

To study the effect of local atomic structure on the core-hole energies of ^{7}Li dopants in Ta, we use Kohn-Sham

DFT, which is a computationally efficient method to investigate the electronic structure of solids [8,9]. In DFT, the many-particle wave function is replaced by a set of single-particle orbitals in a transformation that allows the Hamiltonian of the system to be represented as a functional of the electron density. With this transformation, the kinetic energy of the electrons is approximated by that of a non-interacting system, the electrostatic interactions between electrons are approximated by the Coulomb interactions between electron densities, and an exchange-correlation term is used to account for the remaining electronic energy not included in the kinetic energy and electrostatic interactions. The electron-ion interactions, which connect the electron density to an atomistic description of a solid, normally enter the formulation as an external potential. Over the past several decades, DFT has been extensively used to analyze the electronic structure of a wide variety of materials and predict their physical properties associated with details of their atomic arrangements, resulting in tens of thousands of publications.

Our DFT calculations use the projector-augmented-wave method, as implemented in the Vienna *ab initio* simulation package (VASP) [10–12], with the Perdew-Burke-Ernzerhof exchange-correlation functional [13] and spin polarization included. Pseudopotentials were used containing 13 and 1 valence electrons for Ta and Li, respectively. The crystalline system is obtained from a $5 \times 5 \times 5$ cubic supercell of the bcc structure with 250 Ta atoms and with lattice vectors parallel to the [100], [010], and [001] directions. Wave functions are expanded in a plane-wave basis with a 450-eV energy cutoff. Electronic structure calculations are performed using a $2 \times 2 \times 2$ k-point mesh (Γ centered) with Methfessel-Paxton smearing of width 0.10 eV for Brillouin-zone integrations. The core-hole energy analyses of Li in Ta are based either on a crystalline system with a bcc structure or on an amorphous system. The amorphous structure is constructed based on this 250-atom system and is described in more detail below. All structural optimizations are performed until all forces are below 0.01 eV/Å. For isolated defects or impurities in the Ta lattice, we do not relax the cell volume during structural optimization to model the effects of dilute defects in the Ta bulk without globally perturbing the bulk Ta electronic structure. All core-hole energy calculations are performed by setting the ICORELEVEL tag in VASP to 2. Convergence of total energies and core-hole eigenenergies is performed to 0.1 and 1 meV, respectively.

III. RESULTS

A. Li in crystalline Ta

As a reference case, we initially consider Li dopants in a perfectly crystalline Ta lattice. When deposited on Al, Ta in STJ detectors grows in the bcc phase. Bulk bcc Ta has a lattice constant of $a = 3.30$ Å (we obtain 3.31 Å with DFT), and all Ta atoms have eight nearest neighbors at a distance of $(\sqrt{3}/2)\ a = 2.86$ Å. Interstitial sites at the center of the cube's faces have octahedral symmetry with four in-plane neighbors at a distance of $a/\sqrt{2} = 2.33$ Å and two out-of-plane neighbors at $a/2 = 1.65$ Å [Fig. 2(a)]. In addition, there are two interstitial sites with tetraheral symmetry along each of the midsections of the cube's faces. In the two simplest cases, Li implanted into the Ta lattice can substitute a Ta atom at one of the bcc lattice sites or be located at an octahedral interstitial site [Fig. 2(b)]. Our calculations show that Li is not stable in the tetrahedral interstitial sites and spontaneously moves to the octahedral site with no energy barrier during relaxation. In addition, when Li is placed at the octahedral site in a supercell containing 250 Ta atoms, the two out-of-plane neighbors relax to a nearest-neighbor distance of 2.19 Å, while the four

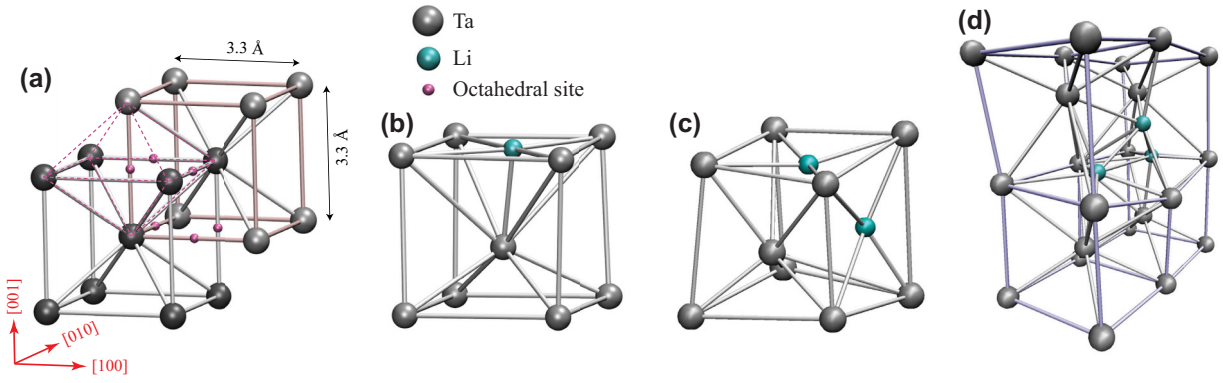

FIG. 2. (a) Bulk Ta has a bcc crystal structure, which is comprised of two intertwined simple cubic lattices, where the corner of one cube is the body center of the other. There are six octahedral interstitial sites per unit cell, which lie at the centers of each face and edge of the cubes; several representative sites are indicated by the small magenta balls. Bcc Ta with (b) one, (c) two, and (d) three clustered Li interstitials are favorable structures, with the associated local lattice distortions shown. (Only portions of the computational supercells are shown for clarity.)

in-plane neighbors move to a distance of 2.39 Å, according to our calculations. With Li on a substitutional site, the Ta lattice relaxes symmetrically around the Li atom and the nearest neigbors are displaced inward by only a small distance of 0.004 Å, even though the atomic radii of Li (1.82 Å) and Ta (2.20 Å) differ considerably.

For each atomic configuration, we calculate the 1s eigenenergies of Li and the associated energy shift relative to the substitutional case, Δ_{1s}, as

$$\Delta_{1s} = E_{1s}^{x} - E_{1s}^{\text{subst}} + \Delta E_{\text{Fermi}} + \Delta V. \quad (1)$$

Here, E_{1s}^{x} and E_{1s}^{subst} are the Li 1s core-hole energies of supercells with Li at site x of interest and with Li at a substitutional site, respectively; ΔE_{Fermi} is the shift in the Fermi levels between these calculations; and ΔV is a correction to appropriately align the electrostatic potentials of the bulk supercell with the electrostatic potential in the bulklike regions of each supercell containing Li. We choose the Li binding energy at a substitutional site as the reference energy throughout this paper. This choice of $E_{1s}^{\text{subst}} = 0$ in Eq. (1) is arbitrary and could be replaced by another reference energy without changing the conclusions. For a single Li ion at an octahedral interstitial site, the 1s binding energy is reduced by 1.18 eV compared to the substitutional Li (Table I). This suggests that core-hole energies are significantly sensitive to the local crystal environment and lattice distortions, even for a well-ordered crystal.

To address the question of whether additional Li ions (from the large ^{7}Li background in the ^{7}Be implantation beam) will settle preferentially near existing Li (Be) implants, we calculate the formation energy, E_f , of a defect according to

$$E_f = E_{\text{Ta,bulk}+n\text{Li}} - E_{\text{Ta,bulk}} + \mu_{\text{Ta}} - \mu_{\text{Li}}. \quad (2)$$

TABLE I. Shift in Li 1s binding energy associated with different lattice incorporation of Li (Be) dopants in crystalline bcc Ta can reach up to 1.67 eV. 1s binding energy for substitutional Li is used as a reference throughout this paper, defining Δ_{1s}(substitutional) = 0 eV in the first row. Formation energies (and defect binding energies) show that (clusters of) Li interstitials are probable, in addition to substitutional Li. Defect complex in the final row consists of a substitutional Li adjacent to a Ta vacancy.

Li site	1s energy shift, Δ_{1s} (eV)	Formation energy, E_f (eV)	Defect binding energy per atom, E_b (eV/Li)
Substitutional	0	1.23	
Single interstitial	1.18	4.07	
Two interstitials	1.58	7.63	–0.26
Three interstitials	1.30	11.23	–0.33
Li_{Ta}–V_{Ta} complex	1.67	2.50	–1.53

Here, $E_{\text{Ta,bulk}}$ is the total energy of the supercell of 250 Ta atoms in a bcc lattice; $E_{\text{Ta,bulk}+n\text{Li}}$ is the total energy after addition of the Li dopants; and μ_{Ta} and μ_{Li} are the chemical potentials of Ta and Li, respectively, given by the number of Ta and Li atoms in the supercell and referenced to the pure metals ($\mu_{\text{Ta}}^0 = -14.30$ eV/atom and $\mu_{\text{Li}}^0 = -1.897$ eV/atom). For our base case of a substitutional Li at a bcc lattice site, the formation energy is $E_f = 1.23$ eV, while at an interstitial site [Fig. 2(b)] it is 4.07 eV (Table I). We also assess the propensity for interstitial clustering by computing the defect binding energy for multiple adjacent Li interstitials (Table I). We define the defect binding energy as the difference in formation energies for the bound versus isolated defects, via $E_b = E_{f,\text{bound}} - \sum E_{f,\text{isolated}}$, where negative values indicate preferred binding. We find that two adjacent Li interstitials are favorable, with a total formation energy that is 3.56 eV higher than the single interstitial and a negative binding energy of –0.26 eV/Li (or –0.51 eV total binding energy). Three clustered Li interstitials are even more energetically favorable compared to three isolated interstitials, with a differential formation energy for the third interstitial of 3.60 eV and a binding energy of –0.33 eV/Li (–0.98 eV total binding energy). These results suggest that Li atoms might accumulate in the vicinity of other Li (Be) dopants. In these models, we consider one of the Li atoms as being associated with the decay of an implanted Be atom, while the others in the cluster represent background implanted Li. Since the implant process also creates vacancies in the Ta lattice (vacancy formation energy of 2.80 eV), we further consider the case of a Li substitutional dopant bound to an adjacent Ta vacancy, the Li_{Ta}–V_{Ta} complex, which is energetically favorable with a binding energy of –1.53 eV (Table I). This vacancy complex is associated with a Li Δ_{1s} shift of 1.67 eV.

Since the binding energies for Li clustering suggest Li may accumulate near other Li (Be) sites and ^{7}Be is accompanied by about 50 times more ^{7}Li atoms during implantation, we also simulate the extreme case, where up to the entire first or second coordination spheres around a ^{7}Be or ^{7}Li dopant are replaced by other ^{7}Li atoms. In these cases, the 1s level does shift further, with the simulations showing $-1.14\ \text{eV} \le \Delta_{1s} \le +0.92$ eV for different configurations of nearest neighbors and a total range of Li 1s binding energies of 2.72 eV.

We further investigate how extreme local strain in the lattice near the implanted atom might further shift the Li 1s binding energy for an otherwise perfect bcc host crystal by displacing the ^{7}Li atom along the [100], [110], or [111] lattice directions without relaxing the host atoms. Displacements up to 1 Å lead to local pressure increases up to about 100 GPa, but yield only $\Delta_{1s} \sim 0.5$ eV. For even larger (unrealistic) displacements, approaching half the equilibrium Ta-Ta distance, we obtain Δ_{1s} less than 2 eV.

Thus, we find that insertion of ^{7}Li atoms into the ordered bcc Ta lattice, depending on whether they are interstitial or substitutional and whether they are clustered, contributes a measurable and significant shift in the 1*s* binding energy of up to 1.7 eV, but it is not sufficient to account for the entire observed 6.7-eV width of the *K*-capture peak of the STJ detectors. The maximum broadening of the electron-capture peaks occurs when the implanted atoms (Li) are segregated inside the Ta lattice, although we have no evidence, so far, that such segregation occurs in the STJ detectors.

B. Li in disordered Ta

We now consider situations in which the Ta matrix is not perfectly crystalline but shows a certain degree of disorder, which is common in sputtered films and following the high-energy implantation process, especially since annealing is not possible in STJ detectors due to potential damage to the thin tunnel barrier. The most common and obvious structural defect is the presence of grain boundaries in polycrystalline films, but dislocations and local disorder from implant-damage tracks may also play a role. Transmission-electron-microscope images of the polycrystalline Ta absorber films in our STJ radiation detectors show average grain sizes of about 20 nm. To understand the change in Li 1*s* core-hole energies at grain boundaries, we consider representative grain-boundary structures of the symmetric (210)[001] ("Σ_5(210)") and (310)[001] ("Σ_3(310)") tilt grain boundaries in Ta [14], both of which have been extensively studied in the literature and from which we obtain the atomic structures [15]. Grain-boundary structures are constructed using the Γ-surface-construction procedure [16], and the low-energy grain-boundary structures identified using this construction are used for the Li core-hole energy analysis here. We place ^{7}Li atoms in four different interstitial sites and four substitutional sites in the vicinity of the grain-boundary planes to sample the variety of local environments and allow the structures to fully relax. For both of these grain boundaries, we find that Δ_{1s} varies between ±0.30 eV for substitutional Li and from −0.30 to +1.65 eV for interstitial Li (Fig. 3).

We also model the effect of dislocations on Li 1*s* core-hole energies. In bcc metals, such as Ta, low-temperature deformation mechanisms are typically governed by the motion of ⟨111⟩/2 screw dislocations, and previous studies have shown that ⟨111⟩/2 dislocations can have different types of core structures [17–19]. For our analysis of core-hole energies, we consider two types of dislocation core structures, easy- and hard-core structures, and they are obtained by applying the continuum-scale elastic displacement field of a screw [20]. The two different core structures correspond to either a positive or a negative displacement field along the [111]-dislocation line direction. Both

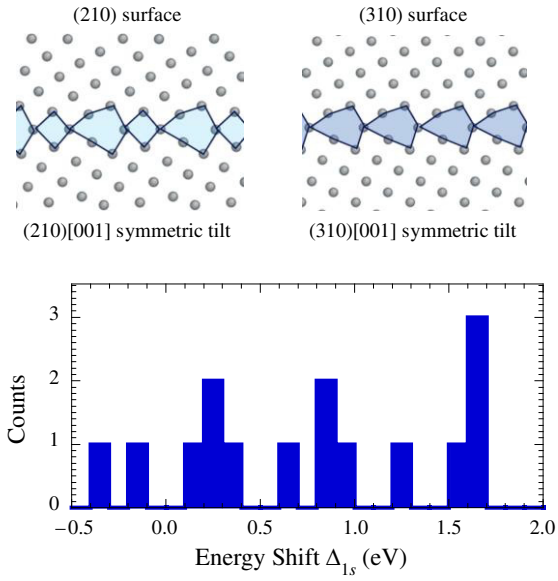

FIG. 3. Top, models of studied grain-boundary structures in Ta. Supercells have dimensions 13.3 × 16.9 × 16.9 Å^3. Bottom, distribution of 1*s* energy shifts, Δ_{1s}, calculated for Li at four different substitutional and four different interstitial sites within the shaded regions of the grain-boundary structures spans –0.3 to 1.65 eV.

of these dislocation core structures preserve the threefold rotation crystal symmetry along the [111] direction parallel to the dislocation line and in bulk Ta. The easy-core structure corresponds to the ground-state configuration, while the hard-core structure has slightly higher energy [21]. Since dislocations are topological defects, two dislocations with opposite Burgers vectors are included in supercells containing 867 atoms (3-Burgers-vectors thick), following the procedure outlined in Ref. [20], to minimize the overall elastic interaction between the dislocations and their periodic replicas. When interstitial and substitutional Li atoms are incorporated into the easy-core dislocation structure, we find that the shifts in Li 1*s* core-hole energies are very small, i.e., in the range of Δ_{1s}= 0.12–0.18 eV. However, when a substitutional Li is placed in the hard-core structure, we find that Δ_{1s}=–0.84 eV. Similarly, when an interstitial Li is inserted into the hard-core structure, we find that Δ_{1s}=–1.62 eV. These high values can be attributed to small Li-Ta distances in the hard-core structure, as close as 1.77 Å for interstitial Li. The Δ_{1s} shifts obtained from the dislocation core structures, analyzed as a function of Li-Ta distance, are comparable to the results obtained from our studies of Li displacements along the ⟨111⟩ direction in the crystalline Ta structure.

To further study the extreme limiting case of disorder, we consider the possibility of fully amorphous structures as an approximate model of local implant damage. We note that fully amorphous structures are not realistic for Ta metal, but we aim here to bound the range of these effects.

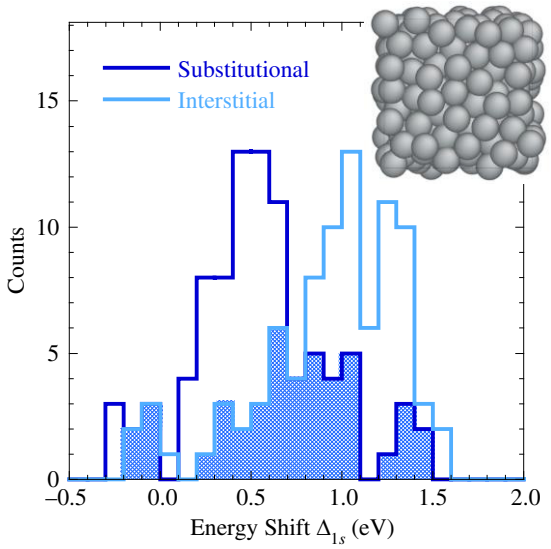

FIG. 4. Distribution of Li 1*s* energy shifts, Δ_{1s}, at 100 substitutional and 100 interstitial sites in amorphous Ta. Inset shows the simulated distribution of Ta atoms after melt quenching and relaxation.

To generate an amorphous Ta distribution, we use a supercell with 250 Ta atoms and perform *ab initio* molecular dynamics melt-quench simulations within the isothermal-isochoric (*NPT*) ensemble using time steps of 1 fs, a Langevin thermostat with a damping coefficient of 10 ps^{-1}, and other parameters as given in Sec. II. The system is heated to 6000 K over 10 ps and thermalized for 4 ps, then quenched to 300 K over 2 ps. The atomic positions are then further relaxed by minimizing the energy of the final structure. The resultant structure exhibits a considerable amount of disorder in the distribution of atomic positions (Fig. 4, inset), although the radial-distribution function indicates weak short-range order (peaks) up to the second-neighbor shell.

To analyze the distribution of core-hole energies for substitutional Li in disordered Ta, we generate 100 structures by randomly replacing one of the Ta atoms with Li and allowing the structure to relax. For interstitial Li in amorphous Ta, we perform a Voronoi tessellation of the amorphous structure and generate 100 structures by placing a Li atom at a randomly selected Voronoi vertex and relaxing the structures. Figure 4 shows the distributions of Li 1*s* core-hole shifts obtained from these 200 structures, which range from –0.3 to 1.6 eV. These values are for fully relaxed structures, including volume relaxation. If, instead, the volumes are constrained to the bulk bcc Ta lattice vectors to approximate local stresses from the implant-damage tracks, we observe nearly rigid shifts of these Δ_{1s} distributions, with the mean Δ_{1s} increasing by about 0.65 eV from an induced pressure of approximately 9 GPa.

Overall, the set of simulations described in this section suggest that locally disordered Ta, which can result from the film-deposition process and/or Be (Li) implantation, results in Li 1*s* energy shifts, Δ_{1s}, between approximately –0.9 and +1.7 eV. Thus, similar to site disorder in the crystalline material, structural disorder of the host Ta can explain a significant fraction of the observed broadening of the *K*-capture peaks but not the full extent.

C. Li with impurities in Ta

Finally, we consider the effect of impurities on the binding energies of the ^{7}Be (^{7}Li) implants. Various impurities are common in the sputtered films and can originate either from impurities in the initial sputter target or can be incorporated from background impurities in the vacuum chamber during deposition, since Ta is a strong getter material. Impurities can also diffuse into the detector during photolithographic processing or storage, or they can originate from contaminants in the implantation beam of the radioactive ^{7}Be dopants, as is the case for the significant background of nonradioactive ^{7}Li. We use time-of-flight secondary-ion mass spectrometry (TOFSIMS) to determine the impurities in the Ta absorber film of the STJ detector used to acquire the spectrum in Fig. 1. TOFSIMS shows that Ta has a uniform distribution of 1200 ppm of Nb, 500 ppm of W, and 300 ppm of In impurities, which likely originate from the initial Ta sputtering target. The quantifications are based on Ta standards with known doses of implanted elements and have an uncertainty of ±20%. In addition, O and C are present at concentrations of 1000 ppm each, and H and Si at 200 ppm. The concentrations of O, C, H, and Si are highest near the surface, suggesting that they diffuse into the Ta film after sputter deposition. Also, O, C, and H may be incorporated during photolithography, and Si may be sputtered off a Si collimator that is placed in front of the wafer during ^{7}Be implantation to define the implantation regions. Additional impurities of F, Na, Cl, Mg, Ca, K, Cr, Mn, Fe, Ni, and Cu are detected in single-digit-ppm trace quantities.

To evaluate the effects on Δ_{1s} due to these impurities, we systematically replace one or more Ta atoms in the first or second coordination spheres around a Li dopant in the crystalline Ta host with one of the elements detected in our Ta films in significant quantities (H, Be, C, N, O, Al, Si, Nb, In). Since there is an almost unlimited number of possible combinations of impurities and configurations, we pick several representative combinations of Li sites and neighboring atoms that are likely to be present in our Ta films. We again further consider some extreme cases to estimate upper limits of the chemical shifts due to impurities. For the extreme cases, we replace the entire coordination shell around a Li site with selected impurities, i.e., either eight impurities in the first or six in the second shell. The computed shifts of the Li 1*s* level for the different combinations of impurity atoms and configurations are summarized in Fig. 5, and a few representative structures

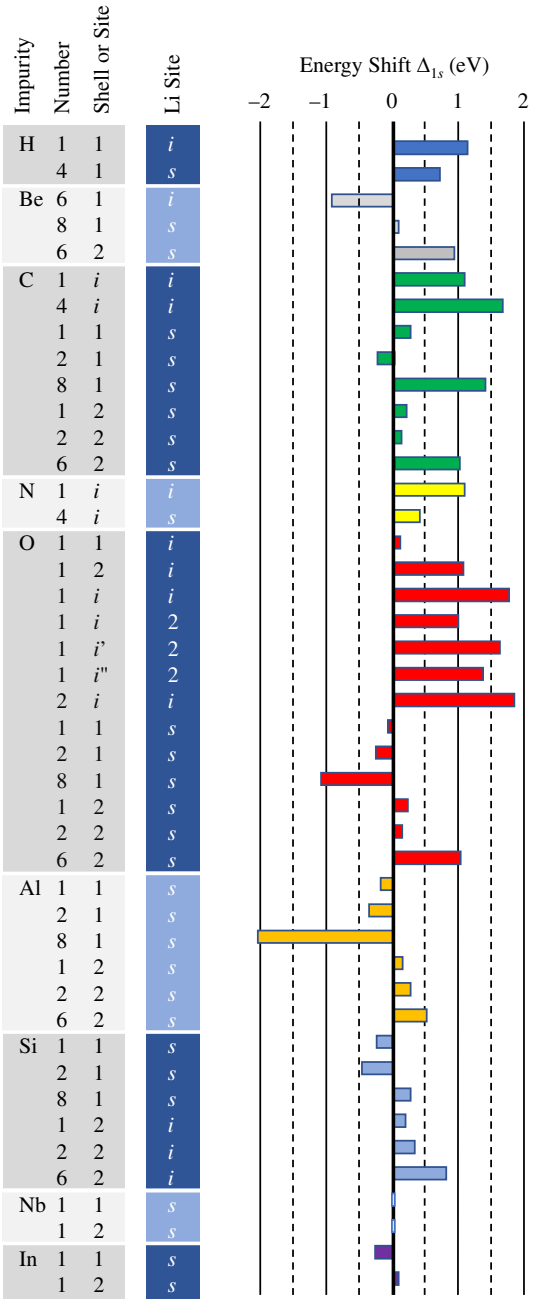

FIG. 5. Energy shifts, Δ_{1s}, of the Li 1*s* level due to different impurities near Li dopant(s). Second column ("Number") indicates the number of impurity atoms of the given element considered for each configuration. Li atoms in substitutional sites are denoted by numbers in the third column ("Shell or Site"), which indicate in which neighbor shell the impurities reside, while interstitial sites are denoted by "*i*." Notation *i* or "*s*" in the fourth column ("Li Site") indicates whether the adjacent Li dopant sits in an interstitial or substitutional site, respectively, while "2" indicates a special configuration with 2 Li dopants in a dumbbell configuration. Notations *i*, *i*′, and *i*″ in the third column, for those O-impurity configurations with the Li dumbbell nearby, refer to different positions of the O impurity in the vicinity of the Li dumbbell. Full neighbor shells consist of 8 or 6 atoms for the first- or second-neighbor shell, respectively.

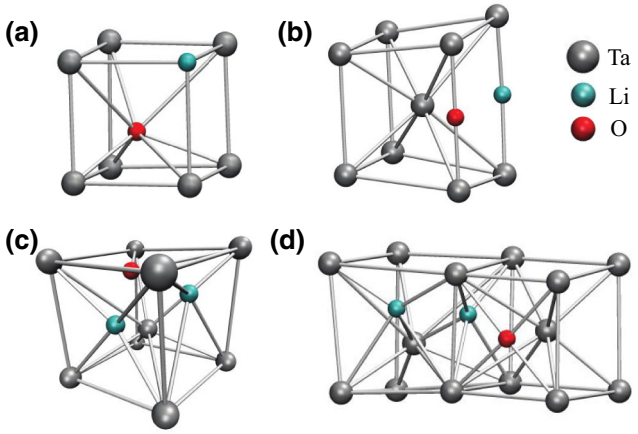

FIG. 6. Representative structures containing an O impurity near implanted Li, showing the local lattice distortions. (a) Li and O on neighboring substitutional sites, (O,1,1,*s*), or row 23 in Fig. 5; (b) Li and O on neighboring interstitial sites, (O,1,*i*,*i*), or row 18 in Fig. 5; (c) Li interstitial dumbbell with neighboring O interstitial, (O,1,*i*,2), or row 19 in Fig. 5; (d) Li interstitial dumbbell with neighboring O interstitial, (O,1,*i*″,2), or row 21 in Fig. 5. (Only portions of the computational supercells are shown for clarity.)

are depicted in Fig. 6. (All atomic structures are available upon request.) Somewhat surprisingly, the range of shifts Δ_{1s} is only about 2 eV for most of the likely impurities and configurations, comparable in magnitude to the shifts for pure Li in different sites of the bcc Ta lattice or even at grain boundaries. The effect is larger for the extreme cases with entire coordination spheres replaced with impurity atoms, extending up to ±2 eV, but this situation is not likely to be present in our detectors, unless there is strong segregation of impurities or the formation of secondary phases. We currently do not have experimental evidence of these occurring, but we cannot completely rule them out. In summary, we find a marginal to appreciable effect on Li 1*s* binding energy in Ta from nearby impurities, but the magnitude of the effects is not likely to broaden the EC peaks significantly beyond the levels caused by structural disorder.

One notable set of observations is related to the effects of oxygen, the influence of which on the Li 1*s* energy differs significantly for interstitial and substitutional sites in the bcc Ta lattice (Fig. 6). In a supercell with a single Li interstitial, e.g., Fig. 6(b), the presence of an O interstitial leads to a large shift, $\Delta_{1s} = 1.76$ eV, in the Li 1*s* core-hole energy. However, in a supercell with two Li interstitials in a dumbbell geometry, e.g., Figs. 6(c) and 6(d), the presence of interstitial O at different positions around the dumbbell causes a shift ranging from 0.97 to 1.62 eV (Fig. 5). Interestingly, when O is located on substitutional Ta lattice sites neighboring Li, the shifts are very small (magnitude less than 0.3 eV). In general, O impurities next to substitutional Li also show small shifts, unless many O atoms

(6 or 8) are clustered around Li. Thus, subtle changes in the position of O impurities around a Li atom can affect the Li 1*s* core-hole energies significantly. This may reflect the tendency of alkaline atoms, such as Li, to form strong bonds with O, the formation of which depends sensitively on their relative distance. Since O is observed to be one of the highest-concentration impurities in our Ta films and shows large variations of the effect on Δ_{1s} depending on configuration, it could dominate the extent of impurity-related *K*-capture peak broadening in the Ta STJs. C, H, and N also show notably large shifts without clustering of impurities.

D. Li 2*s* levels in Ta

Since the observed broadening of the *K*-capture and *L*-capture peaks in the ^{7}Be spectra is different (Fig. 1), we also analyze the effects of site and structural disorder on the Li 2*s* levels in a Ta matrix. The situation for the Li 2*s* levels is fundamentally different from that of 1*s*, since the 2*s* energies overlap with the Ta valence band composed of Ta 5*d* and 6*s* states, and thus, hybridize with the Ta states, creating an inherent broadening. Here, we consider the extent of this broadening and further broadening caused by structural variations of the dopant chemical environment. Figure 7 shows the site-projected electronic density of states (DOS) for Ta, as well as Li at both substitutional and interstitial sites in a crystalline bcc Ta host, in the energy range of the Ta bands near the Fermi level. The Ta DOS we compute is consistent with earlier simulations for pure Ta [22] and does not change significantly for Ta atoms close to a Li defect. The Li 2*s* levels are hybridized with the Ta levels and spread over most of the Ta band of almost 8 eV. However, the extent of strong hybridization (DOS peak) that affects the STJ *L*-capture response function depends on whether Li is incorporated substitutionally or interstitially. Strong hybridization occurs over a significantly broader energy range for interstitial Li (∼5 eV) than substitutional Li (∼2 eV). Overall, this broadening, especially for interstitial Li, is comparable to the observed width of the *L*-capture peak, and this electronic hybridization likely causes it to be broader than the *K*-capture peak, as observed. The Li 2*p* levels also show similar broadening but are less important in the context of the BeEST sterile neutrino search because their wave functions overlap less with the ^{7}Be nucleus, so that their contribution to the *L*-capture signal is negligible.

Finally, we examine how crystalline disorder affects the Li 2*s* levels, using the same methodology as that described in Sec. III B for amorphous Ta structures. Figure 8 shows the corresponding Li 2*s* DOS for a sampling of 35 random substitutional positions in amorphous Ta. The results indicate additional broadening of the substitutional Li 2*s* DOS from atomic disorder, comparable

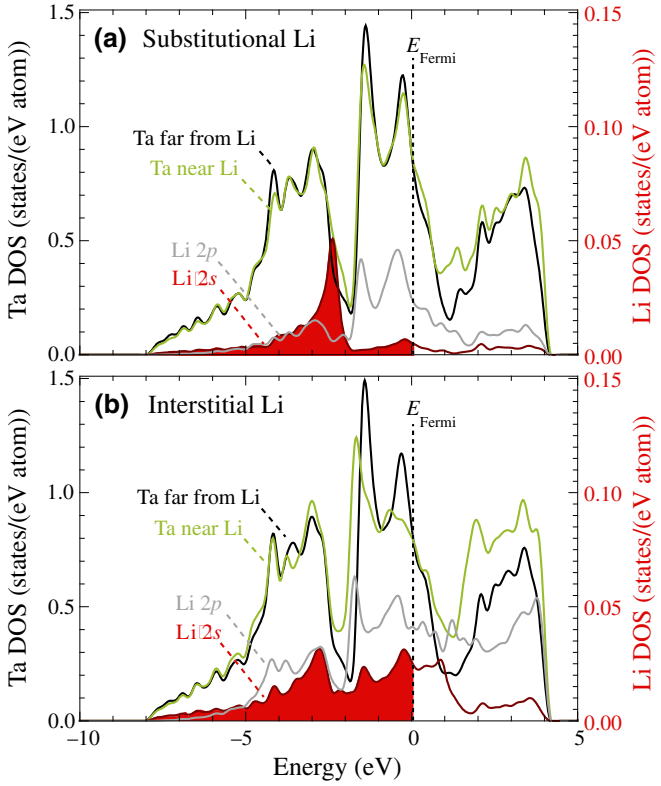

FIG. 7. Density of states of Li 2*s* (red) and 2*p* (gray) atomic levels for (a) substitutional and (b) interstitial Li in a crystalline bcc Ta host show hybridization with the Ta valence band (black and green lines) and consequent broadening. Red shading indicates the occupied portion of the Li 2*s* band, which mainly contributes to the ^{7}Be *L*-capture peak.

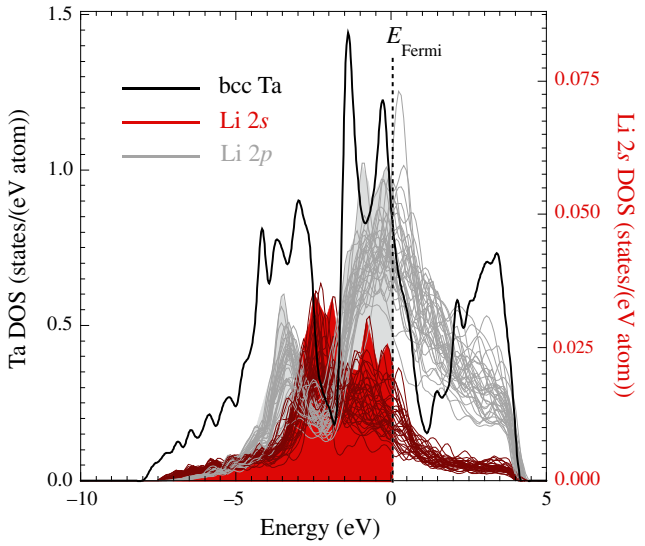

FIG. 8. Density of state of 2*s* (red) and 2*p* (gray) levels for 35 different substitutional Li sites in amorphous Ta. Shaded states below the Fermi energy are occupied, and only the red 2*s* orbitals contribute to the electron-capture process. Compare to the 2*s* DOS for substitutional and interstitial Li in crystalline Ta shown in Fig. 7.

to the extent of hybridization of the interstitial 2*s* DOS in crystalline Ta. Overall, the effects of hybridization are stronger than the effects of lattice disorder, suggesting the *L*-capture peak broadening to be fundamentally limited to a larger value than the *K* capture for ^{7}Be implanted in a metal matrix (e.g., Ta), especially if interstitial implanted dopants are present. The chemical- and material-related effects described above for 1*s* levels and *K* capture, which theoretically can be reduced by atomic level control of the material, do not provide the opportunity to reduce the 2*s*-level (*L* capture) broadening beyond the fundamental limit of the orbital hybridization, which will be present to a different extent for any metal with a DOS extending below the Li 2*s* level (5.4 eV below the Fermi level). This hybridization presents a fundamental lower bound to *L*-capture broadening.

IV. CONCLUSIONS

The impact of chemical shifts on the observed EC spectra of implanted radioisotopes due to the host material is theoretically investigated in detail. For this, we perform DFT simulations of the electronic structure of Li dopants in a polycrystalline Ta matrix relevant to the BeEST experiment. Our work shows that variations in the symmetry and nearest-neighbor configurations of the Li implantation site affect the Li binding energies in a significant way. The energy of the Li 1*s* level differs from the corresponding value for Li in a substitutional site by approximately −0.5 to +1.7 eV for typical site symmetries and dopant concentrations in sputtered Ta films. Somewhat surprisingly, extreme levels of disorder (amorphization) or very high concentrations of impurities (clusters) only increase the range of Li 1*s* energy shifts up to a range of about 4 eV. The Li 2*s* levels are additionally broadened by hybridization with the 5*d* band of the Ta matrix to a width of over 5 eV. These variations in binding energy contribute to broadening of the electron *K*- and *L*-capture peaks from ^{7}Be decay inside Ta-based STJ sensors, because the 1*s* and 2*s* hole energies of the ^{7}Li daughter add to the recoil energy upon relaxation. Such broadening exceeds the STJ detector resolution of 2.0 eV, although the observed broadening (6.7 and 8.2 eV FWHM for the *K*- and *L*-capture peaks, respectively) is larger than that predicted from the material-disorder effects considered here. This suggests these effects to be only one contribution to broadening, although they can explain a significant fraction of the overall effect. Furthermore, hybridization of Li 2*s* with Ta 5*d* orbitals likely causes the *L*-capture peak to be fundamentally broader than the *K*-capture peak in the experimental spectra, with little opportunity for sharpening the *L*-capture peak through extensive material control. We summarize the magnitudes of broadening of the *K*-capture and *L*-capture peaks from the different material effects considered in this work in Tables II and III.

TABLE II. Summary of *K*-capture broadening effects for ^{7}Be decay in Ta matrix from different considered material effects.

Effect	Range of shift or broadening (eV)
Single Li (Be) interstitial in crystalline Ta	+1.2
Multiple Li interstitials in crystalline Ta	+1.3 to +1.6
Substitutional Li in amorphous Ta	–0.3 to +1.5
Interstitial Li in amorphous Ta	–0.2 to +1.6
Li in grain boundary of Ta	–0.4 to +1.6
H impurities	+0.7 to +1.1
Be impurities	–0.95 to +1.0
C impurities	–0.25 to +1.7
N impurities	+0.4 to +1.1
O impurities	–1.1 to +1.8
Al impurities	–2.1 to +0.5
Si impurities	–0.5 to +0.8
Nb impurities	<0.02
In impurities	–0.3 to +0.08

The simulations suggest various approaches to reduce the contribution of material effects to the broadening of the electron-capture spectra. One is to start with ultrapure metals as targets for absorber-film deposition. In addition, electron beam deposition of the STJ electrodes would produce purer films than the current sputtering process. Finally, the absorber film can be annealed after ^{7}Be implantation to remove metastable configurations and place the dopants more uniformly into the energetically most stable substitutional site (Table I). Since STJs cannot be annealed without damaging the tunnel barrier, the dopants must be implanted into the base electrode of the STJ, so that the film can be annealed before the formation of the junction. The relatively long ^{7}Be half-life makes this approach quite feasible. This would also lessen the impact of diffusion of materials into the STJ during storage because the dopants in the base electrode will be well protected.

TABLE III. Summary of *L*-capture broadening effects for ^{7}Be decay in Ta matrix.

Effect	Width of broadening[a] (eV)
Substitutional Li (Be) in crystalline Ta	FWHM ∼ 0.8, FWTM ∼ 2.1
Interstitial Li in crystalline Ta	FWHM ∼ 3.7, FWTM ∼ 6.5
Substitutional Li in amorphous Ta	FWHM ∼ 3.1, FWTM ∼ 4.6

[a]Reported as full width at half maximum (FWHM) and full width at tenth maximum (FWTM) to provide approximate bounds on broadening.

This study quantifies how chemical effects can broaden the EC decay spectra in solid-state radioisotope-doped cryogenic detectors. Understanding this broadening mechanism for ^{7}Li in Ta thin films, in particular, is significant because it currently limits the search for sterile neutrinos in the mass range below 100 keV/c^2 with the BeEST experiment [3]. Our findings suggest that detailed material imaging of the devices to determine the specific environmental conditions for the embedded atoms, combined with these DFT calculations, may allow the sources of spectral broadening to be identified. Furthermore, these theoretical results may also provide a path towards materials engineering of the system in the future to improve the K-capture sensitivity by reducing the in-medium effects and variations in the desired system. Nonetheless, it appears very difficult to limit structural and chemical inhomogeneities to contribute less than an order of 1 eV to the capture peaks in practical devices. Similar broadening will likely also occur, to some extent, in other electron-capture experiments with radioactive isotopes implanted into cryogenic detectors. However, the detailed evaluation of the expected magnitudes in those cases—including later-generation STJs for BeEST and detectors used in other experiments—requires explicit extension of this work to study the specific material systems. Such work is ongoing and will be reported in future publications. Although the relative magnitude of these effects may be smaller in other systems, it is clear that they must be evaluated in detail for experiments of this type to characterize possible systematic uncertainties.

ACKNOWLEDGMENTS

This work is funded by the LLNL LDRD Grant No. 20-LW-006 and the Office of Nuclear Physics in the U.S. Department of Energy's Office of Science under Grant No. DE-SC0021245. This work is performed under the auspices of the U.S. Department of Energy by Lawrence Livermore National Laboratory under Contract No. DE-AC52-07NA27344.

[1] L. Gastaldo, K. Blaum, A. Doerr, Ch. E. Düllmann, K. Eberhardt, S. Eliseev, C. Enss, A. Faessler, A. Fleischmann, S. Kempf, *et al.*, The Electron Capture ^{163}Ho Experiment ECHo, J. Low Temp. Phys. **176**, 876 (2014).

[2] B. Alpert, M. Balata, D. Bennett, M. Biasotti, C. Boragno, C. Brofferio, V. Ceriale, D. Corsini, P. K. Day, M. De Gerone, *et al.*, HOLMES: The electron capture decay of ^{163}Ho to measure the electron neutrino mass with sub-eV sensitivity, Eur. Phys. J. C **75**, 112 (2015).

[3] S. Friedrich, G. B. Kim, C. Bray, R. Cantor, J. Dilling, S. Fretwell, J. A. Hall, A. Lennarz, V. Lordi, P. Machule, *et al.*, Limits on the Existence of sub-MeV Sterile Neutrinos from the Decay of ^{7}Be in Superconducting Quantum Sensors, Phys. Rev. Lett. **126**, 021803 (2021).

[4] S. Fretwell, K. G. Leach, C. Bray, G. B. Kim, J. Dilling, A. Lennarz, X. Mougeot, F. Ponce, C. Ruiz, J. Stackhouse, and S. Friedrich, Direct Measurement of the ^{7}Be L/K Capture Ratio in Ta-Based Superconducting Tunnel Junctions, Phys. Rev. Lett. **125**, 032701 (2020).

[5] M. Drescher, M. Hentschel, R. Kienberger, M. Uiberacker, V. Yakovlev, A. Scrinzi, Th. Westerwalbesloh, U. Kleineberg, U. Heinzmann, and F. Krausz, Time-resolved atomic inner-shell spectroscopy, Nature **419**, 803 (2002).

[6] Y. Blumenfeld, T. Nilsson, and P. van Duppen, Facilities and methods for radioactive ion beam production, Phys. Scr. **T152**, 014023 (2013).

[7] R. Adhikari, M. Agostini, N. Anh Ky, T. Araki, M. Archidiacono, M. Bahr, J. Baur, J. Behrens, F. Bezrukov, P. S. Bhupal Dev, *et al.*, A white paper on keV sterile neutrino dark matter, J. Cosmol. Astropart. Phys. **1**, 025 (2017).

[8] W. Kohn and L. J. Sham, Self-consistent equations including exchange and correlation effects, Phys. Rev. **140**, A1133 (1965).

[9] R. M. Martin, *Electronic Structure: Basic Theory and Practical Methods* (Cambridge University Press, New York, 2008).

[10] G. Kresse and J. Furthmüller, Efficient iterative schemes for *ab initio* total-energy calculations using a plane-wave basis set, Phys. Rev. B **54**, 11169 (1996).

[11] G. Kresse and J. Furthmüller, Efficiency of *ab-initio* total energy calculations for metals and semiconductors using a plane-wave basis set, Comput. Mater. Sci. **6**, 15 (1996).

[12] J. Hafner, *Ab-initio* simulations of materials using VASP: Density-functional theory and beyond, J. Comput. Chem. **29**, 2044 (2008).

[13] J. P. Perdew, K. Burke, and M. Ernzerhof, Generalized Gradient Approximation Made Simple, Phys. Rev. Lett. **77**, 3865 (1996).

[14] A. P. Sutton and R. W. Balluffi, *Interfaces in Crystalline Materials* (Oxford University Press, New York, 1995).

[15] T. Frolov, Q. Zhu, T. Oppelstrup, J. Marian, and R. E. Rudd, Structures and transitions in bcc tungsten grain boundaries and their role in the absorption of point defects, Acta Mater. **159**, 123 (2018).

[16] J. P. Hirth and J. Lothe, *Theory of Dislocations* (Wiley, New York, 1982).

[17] A. S. Argon, *Strengthening Mechanisms in Crystal Plasticity* (Oxford University Press, Oxford, UK, 2008).

[18] D. Rodney and J. Bonneville, in *Physical Metallurgy*, 5th ed., edited by D. Laughlin, K. Hono (Elsevier, Amsterdam, 2014), Vol. II.

[19] V. Vitek, Theory of the core structures of dislocations in body-centered-cubic metals, Cryst. Latt. Defects **5**, 1 (1974).

[20] V. V. Bulatov and W. Cai, *Computer Simulations of Dislocations* (Oxford University Press, New York, 2006).

[21] E. Clouet, L. Ventelon, and F. Willaime, Dislocation Core Energies and Core Fields from First Principles, Phys. Rev. Lett. **102**, 055502 (2009).

[22] L. Boyer, D. A. Papaconstantopoulos, and B. M. Klein, Effect of self-consistency and exchange on the electronic structure of the transition metals, V, Nb, and Ta, Phys. Rev. B **15**, 3685 (1977).